Cell Reports

Mitochondrial membrane tension governs fission

Graphical abstract

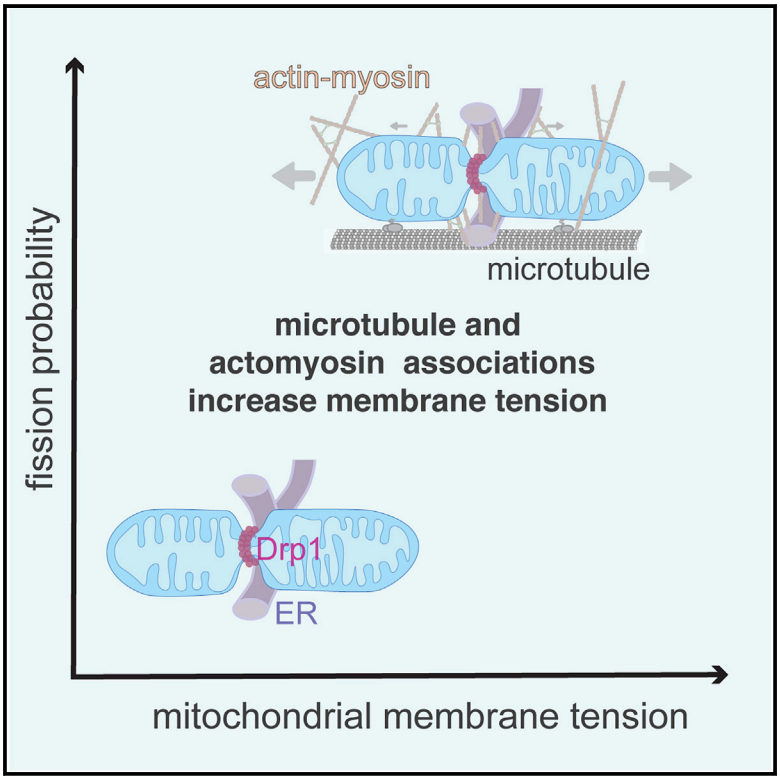

Authors

Dora Mahecic, Lina Carlini, Tatjana Kleele, ..., Stefan Matile, Aurélien Roux, Suliana Manley

Correspondence

suliana.manley@epfl.ch

In brief

Mahecic et al. show that mitochondria constricted by the fission machinery do not always divide. Constricted mitochondria that divide have increased membrane tension compared to those that relax to an unconstricted state. Mitochondrial tension, shown to depend upon microtubules and actomyosin contractility, increases the probability of division.

Highlights

- Mitochondria constricted by canonical fission factors do not invariably divide
- The average tension for mitochondria that divide is higher than for those that do not
- Depolymerizing microtubules or inhibiting myosin II reduces mitochondrial tension
- Probability of division, but not of constriction, depends on mitochondrial tension

Mahecic et al., 2021, Cell Reports *35*, 108947
April 13, 2021
https://doi.org/10.1016/j.celrep.2021.108947

CellPress

Cell Reports

CellPress
OPEN ACCESS

Report

Mitochondrial membrane tension governs fission

Dora Mahecic,[1,2,7] Lina Carlini,[1,2,7] Tatjana Kleele,[1,2] Adai Colom,[2,3,4,5] Antoine Goujon,[2,6] Stefan Matile,[2,6] Aurélien Roux,[2,3] and Suliana Manley[1,2,8,*]

[1]Institute of Physics, École Polytechnique Fédérale de Lausanne (EPFL), Route Cantonale, 1015 Lausanne, Switzerland
[2]National Centre for Competence in Research Programme Chemical Biology, Geneva, Switzerland
[3]Department of Biochemistry, University of Geneva, 1211 Geneva, Switzerland
[4]Biofisika Institute (CSIC, UPV/EHU) and Department of Biochemistry and Molecular Biology, University of the Basque Country, Leioa, Spain
[5]Ikerbasque, Basque Foundation for Science, 48013 Bilbao, Spain
[6]Department of Organic Chemistry, University of Geneva, 1211 Geneva, Switzerland
[7]These authors contributed equally
[8]Lead contact
*Correspondence: suliana.manley@epfl.ch
https://doi.org/10.1016/j.celrep.2021.108947

SUMMARY

During mitochondrial fission, key molecular and cellular factors assemble on the outer mitochondrial membrane, where they coordinate to generate constriction. Constriction sites can eventually divide or reverse upon disassembly of the machinery. However, a role for membrane tension in mitochondrial fission, although speculated, has remained undefined. We capture the dynamics of constricting mitochondria in mammalian cells using live-cell structured illumination microscopy (SIM). By analyzing the diameters of tubules that emerge from mitochondria and implementing a fluorescence lifetime-based mitochondrial membrane tension sensor, we discover that mitochondria are indeed under tension. Under perturbations that reduce mitochondrial tension, constrictions initiate at the same rate, but are less likely to divide. We propose a model based on our estimates of mitochondrial membrane tension and bending energy in living cells which accounts for the observed probability distribution for mitochondrial constrictions to divide.

INTRODUCTION

Mitochondria are highly dynamic organelles, transported through the cytoplasm along cytoskeletal networks while they change in size and shape (Nunnari et al., 1997; Youle and van der Bliek, 2012). Mitochondrial dynamics and network connectivity have been linked to bioenergetic function, allowing the adaptation of cellular energy production in response to stress (Gomes et al., 2011; Rambold et al., 2011; Tondera et al., 2009) and regulation of the cell cycle (Mitra et al., 2009). Mitochondria cannot be generated *de novo*, but instead must proliferate by fission, also referred to as division (Youle and van der Bliek, 2012). Thus, fission plays an important role in ensuring the cellular inheritance of mitochondria, as well as being implicated in quality control by acting as a step in the mitophagic pathway (Burman et al., 2017; Twig et al., 2008).

In mammalian cells, the known mitochondrial fission machinery assembles on the outer surface of the organelle. Initially, the fission site is marked by a pre-constriction defined by contact with endoplasmic reticulum (ER) tubules (Friedman et al., 2011) and deformed by targeted actin polymerization (Ji et al., 2015; Korobova et al., 2013; Manor et al., 2015) and myosin II contraction (Hatch et al., 2014; Korobova et al., 2014; Yang and Svitkina, 2019). Subsequently, surface receptors such as MiD49/51 (Palmer et al., 2011) or Mff (Gandre-Babbe and van der Bliek, 2008; Otera et al., 2010) accumulate at the pre-constriction site and recruit dynamin-related protein (Drp1) (Labrousse et al., 1999; Smirnova et al., 2001). Drp1 oligomerizes into helices that wrap around the division site, and hydrolyzes guanosine triphosphate (GTP) to provide a mechanochemical force for constriction (Fröhlich et al., 2013; Ingerman et al., 2005; Kalia et al., 2018; Mears et al., 2011). In addition, the dynamin 2 protein (Dyn2) can play a role in fission downstream of Drp1 (Lee et al., 2016), albeit a non-essential one (Fonseca et al., 2019; Kamerkar et al., 2018). Interestingly, deformations induced by exogenous mechanical forces can also trigger recruitment of the downstream machinery for mitochondrial fission (Helle et al., 2017). This underlines the fundamentally mechanical nature of membrane fission processes.

An additional factor, membrane tension, is known to play a crucial role in other processes involving membrane deformations such as exocytosis (Gauthier et al., 2011), endocytosis (Morlot et al., 2012; Riggi et al., 2019; Roux et al., 2006), cytokinesis (Lafaurie-Janvore et al., 2013), and cell protrusion (Raucher and Sheetz, 2000). Tension in the plasma membrane is a consequence of built-in bilayer tension and stresses from the cytoskeleton and its motors (Keren et al., 2008; Kozlov and Mogilner, 2007), which together can affect the ability of an applied force to drive membrane fission (Morlot et al., 2012; Roux et al., 2006). In budding yeast, membrane tethers anchoring mitochondria to the cell cortex promote mitochondrial fission, perhaps by increasing membrane tension (Klecker et al., 2013). However,

the role and origins of mitochondrial membrane tension remains little explored in mammalian cells. This is in part because it is challenging to quantify the tension, even in relative terms, in a live-cell context.

Here, we report a key role for membrane tension in governing mitochondrial division in mammalian cells. Using time-lapse super-resolution imaging, we measured dynamic changes in membrane shape to identify highly constricted sites with diameters <200 nm. We observed that the presence of the fission machinery, while necessary, is not sufficient to ensure division. We found that constrictions were more likely to result in division when mitochondria were under higher membrane tension. A fluorescence lifetime imaging microscopy (FLIM) mitochondrial membrane tension sensor (Goujon et al., 2019) revealed that mitochondrial membrane tension was reduced following myosin II inhibition or depolymerization of the microtubule network, a condition that resulted in the same frequency of constriction initiation, but a lower frequency of fissions. Finally, based on our measurements in living cells, we propose a physical model for mitochondrial division in which membrane tension combines with bending energy during constriction to govern the probability of fission.

RESULTS

Constriction by the division machinery does not ensure fission

We performed live-cell structured illumination microscopy (SIM) imaging of COS-7 cells transiently transfected with Drp1-mCherry and GFP targeted to the matrix by the mitochondrial targeting sequence from subunit VIII of human cytochrome *c* oxidase (mito-GFP). We observed that some constrictions marked by Drp1-mCherry proceeded to fission (Figures 1A and S1; Video S1), but others lost enrichment of Drp1 without dividing and relaxed to an unconstricted state ("reversal") (Figures 1B and S1; Video S2). Similar reversible or "non-productive" Drp1 constrictions were previously reported in yeast (Legesse-Miller et al., 2003) and mammalian cells (Ji et al., 2015); however, their cause was unclear. For quantification purposes, we defined reversals as Drp1-enriched constriction sites that reached a diameter <200 nm before relaxing, well below the mean mitochondrial diameter of ~500 nm (Figures 1C, 1D, S1, and S2). Overall, 66% of constriction sites underwent fission (n = 112), while the remaining 34% ended as reversals (n = 57) (Figure S1).

To examine whether reversals result from differences in fission machinery, we imaged several fission factors—the ER, Drp1, and Dyn2. Since our SIM imaging was limited to 2 colors, we performed fast (1 Hz), 3-color live-cell confocal imaging of mitochondria and Drp1, with either Dyn2 or the ER (Figures 1E–1L). We found that Dyn2 could be present or absent at Drp1-mediated constrictions, with 30% of fissions and 36% of reversals enriched in Dyn2 (n = 30 and 33, respectively) (Figures 1I–1L). These observations are consistent with recent reports that Drp1, but not Dyn2, is essential for mitochondrial division (Kamerkar et al., 2018). We further measured colocalization between Drp1-mediated mitochondrial constrictions and ER tubules, as such contacts were shown to mark sites before division (Friedman et al., 2011). We found that both fissions and reversals could occur at constrictions overlapping with ER tubules (90% for fissions, n = 10, and 89% for reversals, n = 18; Figures 1E and 1G), which appear as peaks in intensity profiles along the constriction site (Figures 1F and 1H).

An accumulation of Drp1 at these sites typically coincided with an increased rate of constriction, measured at ~17 nm/s for fissions and 18 nm/s for reversals during the 5 s leading up to maximal constriction (Figure S1; n = 61 for fissions and n = 38 for reversals). Some sites underwent several cycles of constriction and relaxation, coupled with Drp1 accumulation and disassembly (Figure 1D). Cyclic dynamics could lead to either fission or reversal (3 ± 2 constriction cycles/min, n = 61 fissions, and 2 ± 1 cycles/min, n = 38 reversals). Thus, neither abundance of Drp1 nor constriction rate or cyclic activity distinguishes fissions from reversals.

Fission events are characterized by increased membrane tension

Tension can be estimated *in vitro* by pulling on a membrane and measuring the size of the resulting membrane tubule (Derényi et al., 2002; Evans and Yeung, 1994). Analogously, microtubule motors in living cells can spontaneously extrude mitochondrial membrane nanotubes (Huang et al., 2013; Wang et al., 2015) (Figure 2A). We observed nanotubes just before fissions or reversals, at similar frequencies (19% and 24% for n = 101 and n = 59, respectively). We inferred the membrane tension by classical energy minimization, which gives a relationship between the nanotube diameter d, membrane tension τ, and membrane bending rigidity κ_B (Derényi et al., 2002; Evans and Yeung, 1994) (Figure 2B; Method details):

$$\tau = \frac{2\kappa_B}{d^2} \qquad \text{(Equation 1)}$$

The average diameters of tubules pulled from mitochondria that subsequently either divided or reversed were 176 ± 4 and 229 ± 7 nm (mean ± SEM), respectively (Figure 2C). Thus, the population of mitochondria undergoing fission was on average under significantly higher membrane tension at 5.81 ± 0.54 × 10^{-6} N/m, compared to the population undergoing reversals at 3.85 ± 0.75 × 10^{-6} N/m (Figure 2D; n = 19 and n = 14, respectively, means ± SEMs). To independently estimate membrane tension, we examined the motion of dividing mitochondria. We noticed that after division, daughter mitochondria would recoil away from the division site, reminiscent of an elastic body being cut under tension (Figure 2E; Video S3; Method details). We found consistent tension values from analyzing this recoil motion (Method details). Finally, we observed undulations in the shape of some constricting mitochondria (11%, n = 88) (Cho et al., 2017; Gonzalez-Rodriguez et al., 2015), a signature of increased membrane tension, which invariably led to division (100%, n = 10; Figure S3A). These data show that mitochondrial constrictions that are under higher tension are more likely to undergo fission.

Mitochondrial associations with the cytoskeleton modulate membrane tension

Mitochondrial motion depends on actin and microtubule-associated motor proteins that anchor them to the cytoskeleton

CellPress
OPEN ACCESS

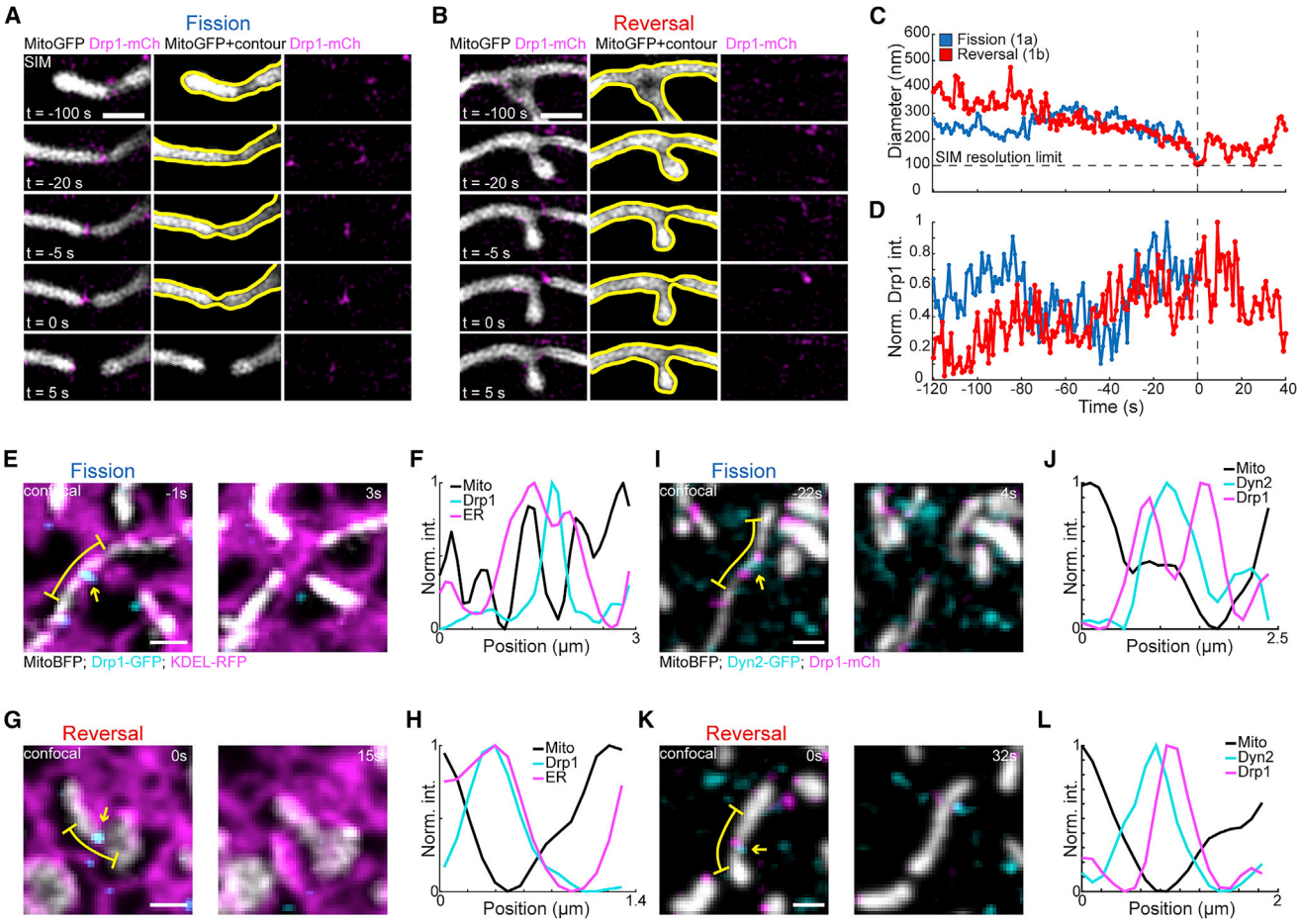

Figure 1. Key molecular components are present at constriction sites that undergo reversals

(A and B) Time-lapse SIM imaging of COS-7 cells transiently transfected with mito-GFP (gray) and mCherry-Drp1 (magenta) showing an example (A) fission and (B) reversal (see Videos S1 and S2).

(C) Mitochondrial constriction site diameter versus time for fission (blue) and reversal (red) events shown in (A) and (B).

(D) Integrated intensity of Drp1 at the constriction site over time measured for fission (blue) and reversal (red) events shown in (A) and (B), normalized to the maximum value.

(E and G) Time-lapse live-cell confocal imaging of Mito-BFP, Drp1-GFP, and KDEL-RFP showing examples of fission and reversal.

(F and H) Intensity profiles of ER, Mito, and Drp1 intensities adjacent to the yellow dashed lines in (E) and (G).

(I and K) Time-lapse SIM imaging of mitochondria and Dyn2 showing a reversal at a Dyn2-enriched constriction site.

(J and L) Intensity profiles of ER, Mito and Drp1 intensities adjacent to the yellow dashed lines in (I) and (K).

Scale bar: 500 nm in (A) and (B). Scale bar: 1 μm in (E), (G), (I), and (K), and yellow arrows mark the constriction site.

(Boldogh and Pon, 2007; Kraft and Lackner, 2018; Yang and Svitkina, 2019); thus, we examined whether these interactions generate mitochondrial membrane tension. To measure tension, we used a mitochondrial-targeted mechanosensitive FliptR probe (Figure S3B) (Colom et al., 2018; Goujon et al., 2019; Soleimanpour et al., 2016). The fluorescence lifetime of FliptR depends on the orientation between its chromophoric groups, which is directly modulated by membrane tension (Figure 3).

We examined the effect of actomyosin contractility on mitochondrial membrane tension by inhibiting myosin II using ML-7 (Saitoh et al., 1987), and measuring the FliptR fluorescence lifetime. FliptR shows a significantly shorter average fluorescence lifetime after ML-7 treatment compared to control cells, which is indicative of a decreased membrane tension (Figures 3A–3C). We independently compared these results with another inhibitor of myosin activity, blebbistatin (Straight et al., 2003), and found again a significant drop in the average fluorescence lifetime (Figure 3C). Washing out blebbistatin or ML-7 showed recovery of the fluorescence lifetime to the level of the untreated control (Figure 3C). Thus, inhibition of myosin activity lowers mitochondrial membrane tension in a reversible manner.

We next investigated the effect of microtubules on mitochondrial membrane tension. First, we performed FLIM imaging with the mitochondria-targeted FliptR probe after depolymerizing microtubules with nocodazole (De Brabander et al., 1976; Hoebeke et al., 1976). In nocodazole-treated cells, FliptR showed significantly shorter average fluorescence lifetimes compared to control values, indicative of an overall reduction in mitochondrial

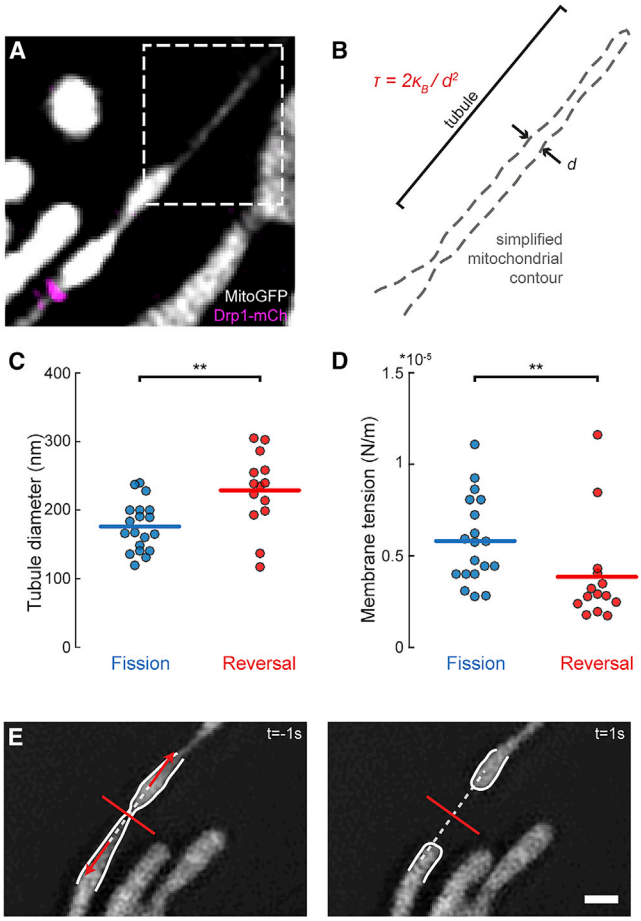

Figure 2. Estimated membrane tension for fissions and reversals

(A) Time-lapse SIM images of a mitochondrion (mito-GFP) 1 s before (left) and after (right) fission showing the recoil of daughter mitochondria post-fission. Measured retraction velocities (red arrows) were projected perpendicular to the constriction site (white dashed line).

(B) Fluorescence image showing a constricted mitochondrion with a pulled membrane tube (boxed region). Scale bar: 1 μm.

(C) Mitochondrial contour from the outlined region in (A) showing the diameter of the tube d, used as a readout for tension τ.

(D) Distribution of tubule radii measured between fission and reversal events.

(E) Distribution of calculated membrane tension values between fission and reversal events.

Statistical significance calculated by 1- or 2-tailed Mann-Whitney *U* test: **p < 0.01.

membrane tension (Figures 3D–3F). Following nocodazole washout, however, mitochondria did not recover their tension over a span of hours and showed reduced mobility (Müller et al., 2005), perhaps due to a residual reduction in mitochondria-microtubule associations. Second, we quantified post-division mitochondrial recoil, post-nocodazole treatment. Although cell and organelle morphologies were maintained (Figures S3C and S3D), we observed a decrease in recoil velocities (Figure 3G) consistent with an estimated reduction in membrane tension of 40% (Method details, n = 33 control and n = 26 nocodazole). These data indicate that mitochondrial membrane tension is reduced in the absence of microtubules.

Having established that nocodazole treatment reduces mitochondrial membrane tension, we examined its impact on mitochondrial division. Importantly, the rate of Drp1-induced constrictions initiated per mitochondrial area was unperturbed by nocodazole treatment (~0.014 min^{-1} μm^{-2}). Furthermore, the degree of overlap between mitochondria and ER remained unchanged (Figures S3C–S3G), as did membrane potential and mitochondrial diameter (Figures S3H and S3I), suggesting that mitochondrial physiology and the ability of the division machinery to constrict were unaffected by nocodazole treatment. However, we found a 2.4-fold increase in the rate of reversal events, and a concomitant decrease in the rate of fission (Figure 3H). Thus, a nocodazole-induced reduction in membrane tension did not change the initiation of Drp1-mediation constrictions, but did reduce their efficiency significantly.

A model for mitochondrial fission: tension modifies the energy landscape

The fission process can be represented as an energy landscape in which the elastic energy stored in the mitochondrial membrane must overcome an energy barrier to fission, E_f. During constriction, the local elastic energy increases through tension and bending of the membrane. To estimate the energy barrier to fission, we used the shape of mitochondrial constrictions (Figures S4A–S4C) to numerically evaluate the Helfrich equation (Helfrich, 1973) (Figures 4 and S4D–S4I; Video S4; Method details). We calculated the probability of fission $p(E)$, defined experimentally as the ratio of the number of fissions to constrictions, for a given bending energy E. $p(E)$ increases with local bending energy, and by determining the bending energy at which all constrictions result in fission ($p(E) = 1$), we could estimate the energy barrier to fission as ~300 k_BT. This is a lower bound, considering that higher curvatures would be obscured by our limited spatial resolution. Nevertheless, considering that mitochondria are double-membraned organelles, this estimate is consistent with simulations of dynamin-mediated scission (Morlot et al., 2012), as well as theoretical estimates for a hemifission state, which spontaneously leads to fission (Kozlovsky and Kozlov, 2003).

To test the effect of membrane tension on the energy landscape for fission, we compared the experimental probability of fission between control and nocodazole-treated cells. We found that higher bending energies were required when membrane tension is reduced (Figure 4B). Therefore, achieving a similar probability of fission would now require more deformation to overcome the energy barrier (Figure 4C; n = 33 control and 22 nocodazole). We also noticed that Drp1 appeared to reside for longer time periods at mitochondrial constriction sites in nocodazole-treated cells. Fission events in nocodazole-treated cells required on average ~12 ± 7 s longer (mean ± SEM; Figure 4D; n = 33 control and n = 22 nocodazole), reflecting decreased fission probability and consistent with a major role for membrane tension in driving the final step of fission.

DISCUSSION

We report that membrane tension plays a key role in governing mitochondrial fission. What sets membrane tension?

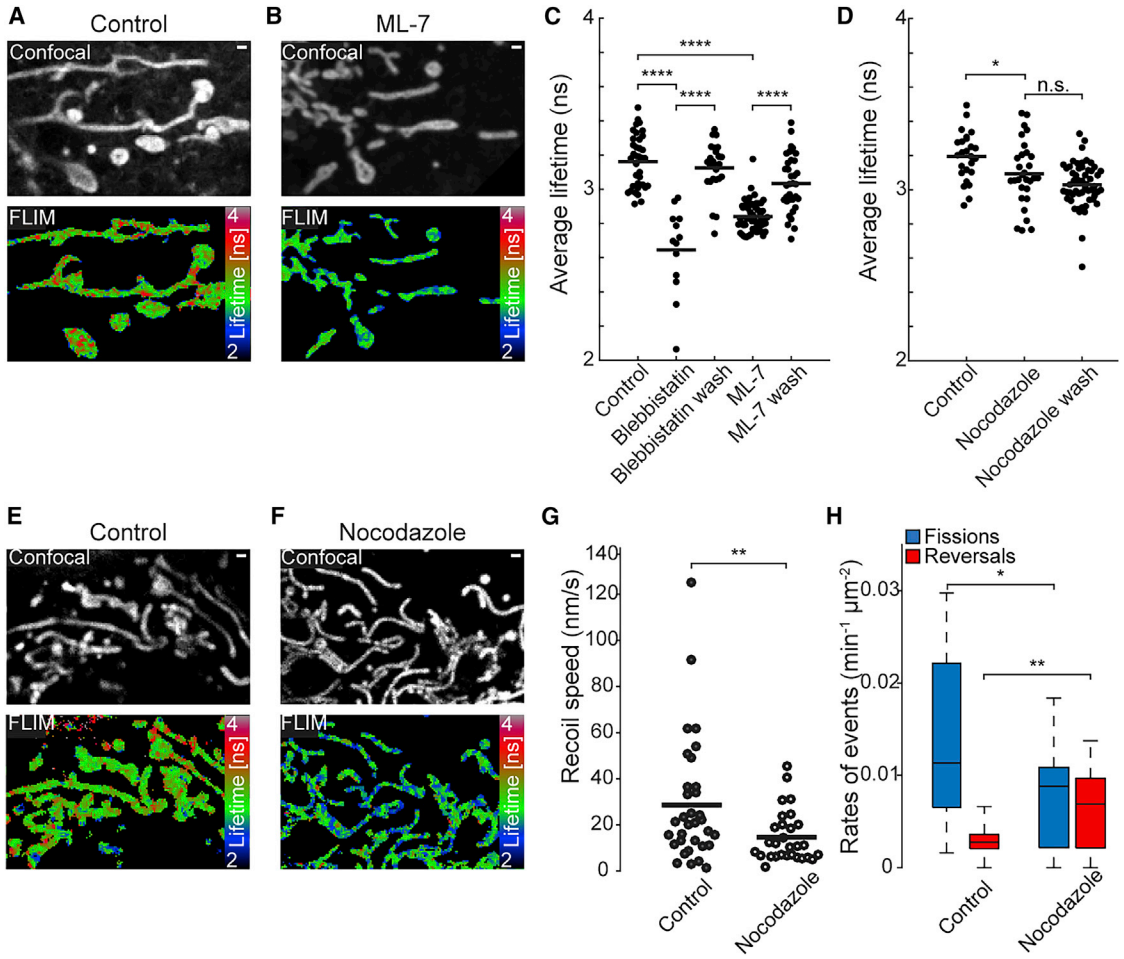

Figure 3. Membrane tension under perturbations to the cytoskeleton

(A and B) Confocal (top) and FLIM (bottom) images of mitochondria in cells stained with the mitochondria-targeted FliptR fluorescent tension probe under (A) control conditions and (B) ML-7 treatment.

(C) Distributions of average fluorescence lifetimes of the FliptR fluorescent tension probe between control, blebbistatin-treated cells, ML-7-treated cells, and washouts.

(D) Distributions of bulk average fluorescence lifetimes of the FliptR fluorescent tension probe between control and nocodazole-treated cells.

(E and F) Confocal (top) and FLIM (bottom) images of mitochondria in cells stained with the mitochondria-targeted FliptR fluorescent tension probe under (E) control conditions and (F) nocodazole treatment.

(G) Distribution of recoil speeds of mitochondria post-division, between control and nocodazole treated cells.

(H) Box chart showing rates of fission and reversal in nocodazole treated (n = 16) and control (n = 16) cells (SIM videos with 6-s temporal resolution). The central line marks the median, and the bottom and top of the box mark the 25th and 75th percentiles, respectively.

Scale bars: 1 μm. Line marks the mean of the distribution. Statistical significance calculated by 1- or 2-tailed Mann-Whitney U test: *$p < 0.05$, **$p < 0.01$, ****$p < 0.0001$, n.s., not significant.

Microtubule-based motor proteins are largely responsible for mitochondrial transport in mammalian cells (Boldogh and Pon, 2007; Moore and Holzbaur, 2018), and the piconewton forces exerted by these motor proteins are sufficient to induce tension by locally pulling or anchoring mitochondria. In addition, the actomyosin network, which constricts mitochondria and regulates Drp1 recruitment (Chakrabarti et al., 2018; Ji et al., 2015; Korobova et al., 2014; Manor et al., 2015), accumulates at the division site (Yang and Svitkina, 2019). Thus, cytoskeletal networks may locally regulate mitochondrial membrane tension, possibly through stochastic contractility.

How might tension promote mitochondrial division? Elastic energy due to constriction from the division machinery, combined with tension, brings membranes closer to fission (Figures 4E and 4F). In a model proposed for dynamin-mediated endocytosis, thermal fluctuations of the membrane overcome the energy barrier to fission (Morlot et al., 2012). We propose that that tension fluctuations could play an analogous role for mitochondria. Both microtubule- and actin-dependent motor proteins can generate piconewtons of force on millisecond timescales (Carter and Cross, 2005; Finer et al., 1994). This suggests that tension may be modulated several orders of magnitude

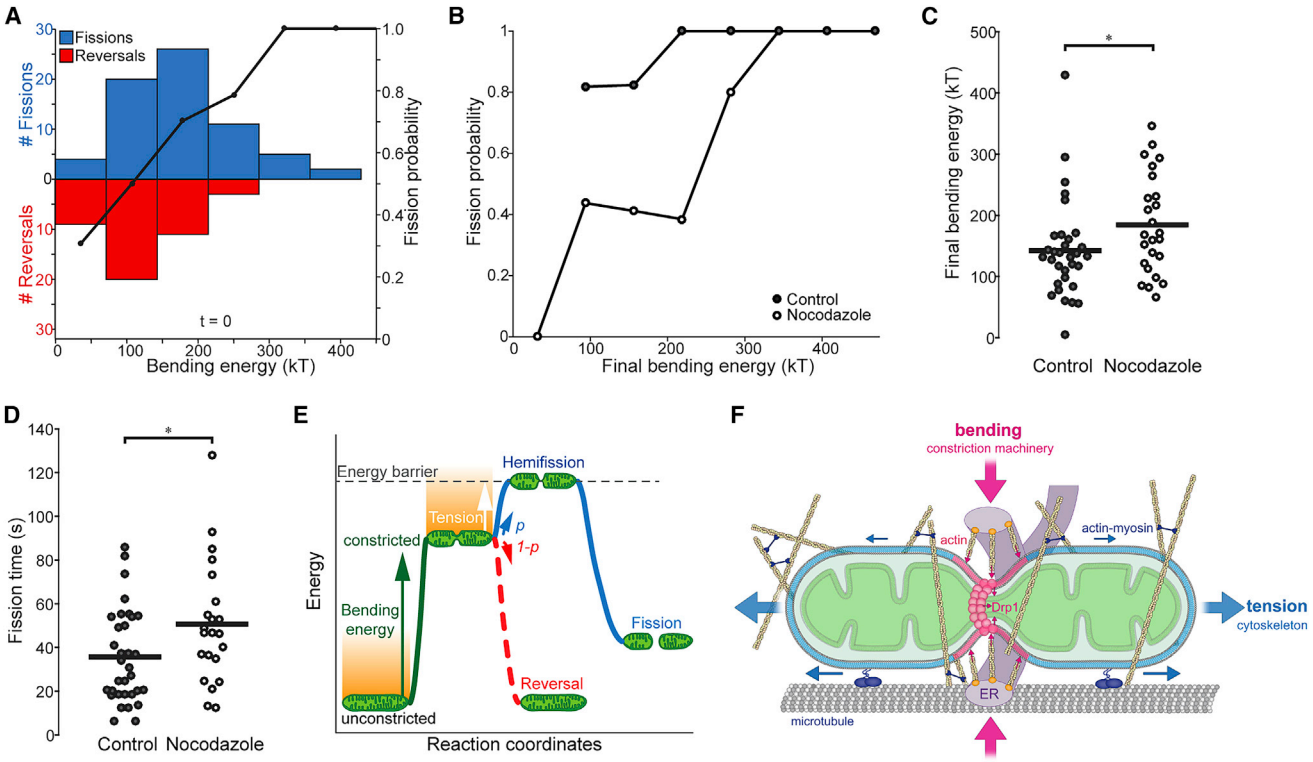

Figure 4. Fission timing and probability related to bending energy and tension

(A) Left: histogram of fissions and reversals at different local bending energy intervals. Right: experimental probability of fission at different local bending energy intervals.

(B) Experimental probability of fission of control and nocodazole-treated cells.

(C) Distribution of final bending energies between control and nocodazole-treated fission events.

(D) Distribution of fission times between control and nocodazole-treated fission events.

(E) Illustration of the probabilistic model of mitochondrial fission showing the contribution of bending energy (green line) and membrane tension (orange-shaded area) in reaching the energy barrier for fission (gray dashed line). Both bending energy and tension set the probability p of fission (blue line). Reversals occur either due to a lack of bending energy or the low probability of necessary fluctuation energies.

(F) Schematic representation of the different contributions to fission probability: bending energy (magenta) and tension (blue).

Line marks the mean of the distribution. Statistical significance calculated by 1- or 2-tailed Mann-Whitney U test: *$p < 0.05$.

faster than it takes a mitochondrion to divide. Fluctuations in tension could then stochastically deform mitochondrial membranes, storing additional elastic energy at the constriction site to overcome the energy barrier to fission. According to such a model, since constrictions cannot be maintained indefinitely, mitochondrial constriction sites that do not experience a large enough fluctuation during their lifetime will become reversals. This model is supported by our independent estimates of the energy contribution from tension and the magnitude of the mean fluctuation energy extracted from the experimental probability of fission, both of which are ~50 k_BT, far greater than thermal fluctuations (Method details). Consistent with the proposed role for the cytoskeleton in generating tension, mitochondria in nocodazole-treated cells have an elevated probability of reversals.

The role of tension in mitochondrial fission may contribute to mitochondrial genome maintenance and distribution across the network. For instance, mitochondrial division has been observed to take place near replicating nucleoids (Lewis et al., 2016), the presence of which may create "rigid islands" that alter the mechanical properties at adjacent constriction sites (Feng and Kornmann, 2018), making them more likely to divide according to our model. Such internal mechanisms could simultaneously control the position and fate of mitochondrial constrictions. Furthermore, our work suggests that cytoskeletal remodeling could affect global mitochondrial proliferation through modulating mitochondrial membrane tension. This is consistent with the strong dependence of mitochondrial network morphology on the cell cycle, although direct mechanisms remain to be discovered.

STAR★METHODS

Detailed methods are provided in the online version of this paper and include the following:

- KEY RESOURCES TABLE
- RESOURCE AVAILABILITY

SUPPLEMENTAL INFORMATION

Supplemental information can be found online at https://doi.org/10.1016/j.celrep.2021.108947.

ACKNOWLEDGMENTS

We thank Caterina Tomba for help with FLIM imaging, Hélène Perreten for technical support, Hari Shroff for the mitoGFP construct, and Gia Voeltz for the Drp1 and Dyn2 constructs. Imaging data used in this publication were produced in collaboration with the Advanced Imaging Center, a facility jointly supported by the Gordon and Betty Moore Foundation and HHMI at HHMI's Janelia Research Campus. We thank Lin Shao and Teng-Leong Chew at Janelia AIC for their help with SIM imaging, and Thierry Laroche at EPFL-BIOP. We thank Niklas Berliner, Jennifer Lippincott-Schwartz, Simon Schutz, and Tobias Schneider for helpful discussions. We thank Timo Rey, Sofia Zaganelli, Benoit Kornmann, Qian Feng, Thomas Misgeld, and Leanne Godinho for comments on the manuscript. This work was supported in part by the National Centre of Competence in Research Chemical Biology (S. Manley, S. Matile, and A.R.). S. Manley also acknowledges SNSF Project Grant 31003A_182429 (to T.K. and D.M). T.K. received funding from the European Molecular Biology Organization (ALTF-739-2016) and the Munich Cluster for Systems Neurology (SyNergy). A.C. received funding from MCIU, MINECOG19/P66, RYC-18/02, and T1270-19.

AUTHOR CONTRIBUTIONS

Conceptualization, D.M., L.C., T.K., A.R., and S. Manley; methodology, D.M., L.C., T.K., A.R., and S. Manley; software, D.M. and L.C.; validation, D.M., L.C., and T.K.; formal analysis, D.M., L.C., and A.C.; investigation, D.M., L.C., T.K., and A.C.; resources, A.C., A.G., S. Matile, and A.R.; data curation, D.M. and L.C.; writing – original draft, D.M., L.C., and S. Manley; writing – review and editing, D.M., L.C., T.K., A.C., A.G., S. Matile, A.R., and S. Manley; visualization, D.M., L.C., and T.K.; supervision, A.R. and S. Manley; project administration, S. Manley; funding acquisition, S. Matile, A.R., A.C., T.K. and S. Manley.

DECLARATION OF INTERESTS

The University of Geneva has licensed four Flipper-TR probes to Spirochrome for commercialization.

Received: July 27, 2020
Revised: December 15, 2020
Accepted: March 14, 2021
Published: April 13, 2021

REFERENCES

Alharbi, K.A. (2013). Image fusion superresolution in structured illumination microscopy. PhD thesis (California State University).

Arganda-Carreras, I., Cardona, A., Kaynig, V., and Schindelin, J. (2017). Trainable Weka Segmentation: A Machine Learning Tool for Microscopy Image Segmentation. Bioinformatics *33*, 2424–2426.

Boldogh, I.R., and Pon, L.A. (2007). Mitochondria on the move. Trends Cell Biol. *17*, 502–510.

Burman, J.L., Pickles, S., Wang, C., Sekine, S., Vargas, J.N.S., Zhang, Z., Youle, A.M., Nezich, C.L., Wu, X., Hammer, J.A., and Youle, R.J. (2017). Mitochondrial fission facilitates the selective mitophagy of protein aggregates. J. Cell Biol. *216*, 3231–3247.

Cardillo, G. (2015). Mwwtest. https://www.mathworks.com/matlabcentral/fileexchange/25830-mwwtest.

Carter, N.J., and Cross, R.A. (2005). Mechanics of the kinesin step. Nature *435*, 308–312.

Chakrabarti, R., Ji, W.K., Stan, R.V., de Juan Sanz, J., Ryan, T.A., and Higgs, H.N. (2018). INF2-mediated actin polymerization at the ER stimulates mitochondrial calcium uptake, inner membrane constriction, and division. J. Cell Biol. *217*, 251–268.

Chan, T.F., and Vese, L.A. (2001). Active contours without edges. IEEE Trans. Image Process. *10*, 266–277.

Cho, B., Cho, H.M., Jo, Y., Kim, H.D., Song, M., Moon, C., Kim, H., Kim, K., Sesaki, H., Rhyu, I.J., et al. (2017). Constriction of the mitochondrial inner compartment is a priming event for mitochondrial division. Nat. Commun. *8*, 15754.

Colom, A., Derivery, E., Soleimanpour, S., Tomba, C., Molin, M.D., Sakai, N., González-Gaitán, M., Matile, S., and Roux, A. (2018). A fluorescent membrane tension probe. Nat. Chem. *10*, 1118–1125.

Curd, A., Cleasby, A., Makowska, K., York, A., Shroff, H., and Peckham, M. (2015). Construction of an instant structured illumination microscope. Methods *88*, 37–47.

De Brabander, M.J., Van de Veire, R.M.L., Aerts, F.E.M., Borgers, M., and Janssen, P.A. (1976). The effects of methyl (5-(2-thienylcarbonyl)-1H-benzimidazol-2-yl) carbamate, (R 17934; NSC 238159), a new synthetic antitumoral drug interfering with microtubules, on mammalian cells cultured in vitro. Cancer Res. *36*, 905–916.

Derényi, I., Jülicher, F., and Prost, J. (2002). Formation and interaction of membrane tubes. Phys. Rev. Lett. *88*, 238101.

Donzeau, M., Káldi, K., Adam, A., Paschen, S., Wanner, G., Guiard, B., Bauer, M.F., Neupert, W., and Brunner, M. (2000). Tim23 links the inner and outer mitochondrial membranes. Cell *101*, 401–412.

Evans, E., and Yeung, A. (1994). Hidden dynamics in rapid changes of bilayer shape. Chem. Phys. Lipids *73*, 39–56.

Feng, Q., and Kornmann, B. (2018). Mechanical forces on cellular organelles. J. Cell Sci. *131*, jcs218479.

Finer, J.T., Simmons, R.M., and Spudich, J.A. (1994). Single myosin molecule mechanics: piconewton forces and nanometre steps. Nature *368*, 113–119.

Fiolka, R., Shao, L., Rego, E.H., Davidson, M.W., and Gustafsson, M.G.L. (2012). Time-lapse two-color 3D imaging of live cells with doubled resolution using structured illumination. Proc. Natl. Acad. Sci. USA *109*, 5311–5315.

Fonseca, T.B., Sánchez-Guerrero, Á., Milosevic, I., and Raimundo, N. (2019). Mitochondrial fission requires DRP1 but not dynamins. Nature *570*, E34–E42.

Friedman, J.R., Lackner, L.L., West, M., DiBenedetto, J.R., Nunnari, J., and Voeltz, G.K. (2011). ER tubules mark sites of mitochondrial division. Science *334*, 358–362.

Fröhlich, C., Grabiger, S., Schwefel, D., Faelber, K., Rosenbaum, E., Mears, J., Rocks, O., and Daumke, O. (2013). Structural insights into oligomerization and mitochondrial remodelling of dynamin 1-like protein. EMBO J. *32*, 1280–1292.

Gandre-Babbe, S., and van der Bliek, A.M. (2008). The novel tail-anchored membrane protein Mff controls mitochondrial and peroxisomal fission in mammalian cells. Mol. Biol. Cell *19*, 2402–2412.

Gauthier, N.C., Fardin, M.A., Roca-Cusachs, P., and Sheetz, M.P. (2011). Temporary increase in plasma membrane tension coordinates the activation of exocytosis and contraction during cell spreading. Proc. Natl. Acad. Sci. USA *108*, 14467–14472.

Gomes, L.C., Di Benedetto, G., and Scorrano, L. (2011). During autophagy mitochondria elongate, are spared from degradation and sustain cell viability. Nat. Cell Biol. *13*, 589–598.

Gonzalez-Rodriguez, D., Sart, S., Babataheri, A., Tareste, D., Barakat, A.I., Clanet, C., and Husson, J. (2015). Elastocapillary Instability in Mitochondrial Fission. Phys. Rev. Lett. *115*, 088102.

Goujon, A., Colom, A., Straková, K., Mercier, V., Mahecic, D., Manley, S., Sakai, N., Roux, A., and Matile, S. (2019). Mechanosensitive Fluorescent Probes to Image Membrane Tension in Mitochondria, Endoplasmic Reticulum, and Lysosomes. J. Am. Chem. Soc. *141*, 3380–3384.

Gustafsson, M.G.L. (2000). Surpassing the lateral resolution limit by a factor of two using structured illumination microscopy. J. Microsc. *198*, 82–87.

Gustafsson, M.G.L., Shao, L., Carlton, P.M., Wang, C.J.R., Golubovskaya, I.N., Cande, W.Z., Agard, D.A., and Sedat, J.W. (2008). Three-dimensional resolution doubling in wide-field fluorescence microscopy by structured illumination. Biophys. J. *94*, 4957–4970.

Hatch, A.L., Gurel, P.S., and Higgs, H.N. (2014). Novel roles for actin in mitochondrial fission. J. Cell Sci. *127*, 4549–4560.

Helfrich, W. (1973). Elastic properties of lipid bilayers: theory and possible experiments. Z. Naturforsch. C *28*, 693–703.

Helle, S.C.J., Feng, Q., Aebersold, M.J., Hirt, L., Grüter, R.R., Vahid, A., Sirianni, A., Mostowy, S., Snedeker, J.G., Šarić, A., et al. (2017). Mechanical force induces mitochondrial fission. eLife *6*, e30292.

Hoebeke, J., Van Nijen, G., and De Brabander, M. (1976). Interaction of oncodazole (R 17934), a new antitumoral drug, with rat brain tubulin. Biochem. Biophys. Res. Commun. *69*, 319–324.

Hu, G.B. (2014). Whole cell cryo-electron tomography suggests mitochondria divide by budding. Microsc. Microanal. *20*, 1180–1187.

Huang, X., Sun, L., Ji, S., Zhao, T., Zhang, W., Xu, J., Zhang, J., Wang, Y., Wang, X., Franzini-Armstrong, C., et al. (2013). Kissing and nanotunneling mediate intermitochondrial communication in the heart. Proc. Natl. Acad. Sci. USA *110*, 2846–2851.

Ingerman, E., Perkins, E.M., Marino, M., Mears, J.A., McCaffery, J.M., Hinshaw, J.E., and Nunnari, J. (2005). Dnm1 forms spirals that are structurally tailored to fit mitochondria. J. Cell Biol. *170*, 1021–1027.

Ji, W.K., Hatch, A.L., Merrill, R.A., Strack, S., and Higgs, H.N. (2015). Actin filaments target the oligomeric maturation of the dynamin GTPase Drp1 to mitochondrial fission sites. eLife *4*, e11553.

Jim. (2015). Least-squares smoother. https://www.mathworks.com/matlabcentral/fileexchange/49789-least-squares-smoother.

Kalia, R., Wang, R.Y.-R.R., Yusuf, A., Thomas, P.V., Agard, D.A., Shaw, J.M., and Frost, A. (2018). Structural basis of mitochondrial receptor binding and constriction by DRP1. Nature *558*, 401–405.

Kamerkar, S.C., Kraus, F., Sharpe, A.J., Pucadyil, T.J., and Ryan, M.T. (2018). Dynamin-related protein 1 has membrane constricting and severing abilities sufficient for mitochondrial and peroxisomal fission. Nat. Commun. *9*, 5239.

Keren, K., Pincus, Z., Allen, G.M., Barnhart, E.L., Marriott, G., Mogilner, A., and Theriot, J.A. (2008). Mechanism of shape determination in motile cells. Nature *453*, 475–480.

Klecker, T., Scholz, D., Förtsch, J., and Westermann, B. (2013). The yeast cell cortical protein Num1 integrates mitochondrial dynamics into cellular architecture. J. Cell Sci. *126*, 2924–2930.

Korobova, F., Ramabhadran, V., and Higgs, H.N. (2013). An Actin-Dependent Step in Mitochondrial Fission Mediated by the ER-Associated Formin INF2. Science *339*, 464–467.

Korobova, F., Gauvin, T.J., and Higgs, H.N. (2014). A role for myosin II in mammalian mitochondrial fission. Curr. Biol. *24*, 409–414.

Kozlov, M.M., and Mogilner, A. (2007). Model of polarization and bistability of cell fragments. Biophys. J. *93*, 3811–3819.

Kozlovsky, Y., and Kozlov, M.M. (2003). Membrane fission: model for intermediate structures. Biophys. J. *85*, 85–96.

Kraft, L.M., and Lackner, L.L. (2018). Mitochondrial anchors: positioning mitochondria and more. Biochem. Biophys. Res. Commun. *500*, 2–8.

Kroon, D.-J. (2011). 2D line curvature and normals. https://www.mathworks.com/matlabcentral/fileexchange/32696-2d-line-curvature-and-normals.

Labrousse, A.M., Zappaterra, M.D., Rube, D.A., and van der Bliek, A.M. (1999). C. elegans dynamin-related protein DRP-1 controls severing of the mitochondrial outer membrane. Mol. Cell *4*, 815–826.

Lafaurie-Janvore, J., Maiuri, P., Wang, I., Pinot, M., Manneville, J.-B., Betz, T., Balland, M., and Piel, M. (2013). ESCRT-III Assembly and Cytokinetic Abscission Are Induced by Tension Release in the Intercellular Bridge. Science *339*, 1625–1629.

Lee, J.E., Westrate, L.M., Wu, H., Page, C., and Voeltz, G.K. (2016). Multiple dynamin family members collaborate to drive mitochondrial division. Nature *540*, 139–143.

Legesse-Miller, A., Massol, R.H., and Kirchhausen, T. (2003). Constriction and Dnm1p recruitment are distinct processes in mitochondrial fission. Mol. Biol. Cell *14*, 1953–1963.

Lewis, S.C., Uchiyama, L.F., and Nunnari, J. (2016). ER-mitochondria contacts couple mtDNA synthesis with Mitochondrial division in human cells. Science *353*, aaf5549.

Liu, T., Liu, X., Spring, D.R., Qian, X., Cui, J., and Xu, Z. (2014). Quantitatively mapping cellular viscosity with detailed organelle information via a designed PET fluorescent probe. Sci. Rep. *4*, 5418.

Lucy, L.B. (1974). An iterative technique for the rectification of observed distributions. Astron. J. *79*, 745.

Manor, U., Bartholomew, S., Golani, G., Christenson, E., Kozlov, M., Higgs, H., Spudich, J., and Lippincott-Schwartz, J. (2015). A mitochondria-anchored isoform of the actin-nucleating spire protein regulates mitochondrial division. eLife *4*, e08828.

Mears, J.A., Lackner, L.L., Fang, S., Ingerman, E., Nunnari, J., and Hinshaw, J.E. (2011). Conformational changes in Dnm1 support a contractile mechanism for mitochondrial fission. Nat. Struct. Mol. Biol. *18*, 20–26.

Mitra, K., Wunder, C., Roysam, B., Lin, G., and Lippincott-Schwartz, J. (2009). A hyperfused mitochondrial state achieved at G1-S regulates cyclin E buildup and entry into S phase. Proc. Natl. Acad. Sci. USA *106*, 11960–11965.

Moore, A.S., and Holzbaur, E.L.F. (2018). Mitochondrial-cytoskeletal interactions: dynamic associations that facilitate network function and remodeling. Curr. Opin. Physiol. *3*, 94–100.

Morlot, S., Galli, V., Klein, M., Chiaruttini, N., Manzi, J., Humbert, F., Dinis, L., Lenz, M., Cappello, G., and Roux, A. (2012). Membrane shape at the edge of the dynamin helix sets location and duration of the fission reaction. Cell *151*, 619–629.

Müller, M., Mironov, S.L., Ivannikov, M.V., Schmidt, J., and Richter, D.W. (2005). Mitochondrial organization and motility probed by two-photon microscopy in cultured mouse brainstem neurons. Exp. Cell Res. *303*, 114–127.

Niggemann, G., Kummrow, M., and Helfrich, W. (1995). The Bending Rigidity of Phosphatidylcholine Bilayers - Dependences on Experimental-Method, Sample Cell Sealing and Temperature. J. Phys. II France *5*, 413–425.

Nunnari, J., Marshall, W.F., Straight, A., Murray, A., Sedat, J.W., and Walter, P. (1997). Mitochondrial transmission during mating in Saccharomyces cerevisiae is determined by mitochondrial fusion and fission and the intramitochondrial segregation of mitochondrial DNA. Mol. Biol. Cell *8*, 1233–1242.

Otera, H., Wang, C., Cleland, M.M., Setoguchi, K., Yokota, S., Youle, R.J., and Mihara, K. (2010). Mff is an essential factor for mitochondrial recruitment of Drp1 during mitochondrial fission in mammalian cells. J. Cell Biol. *191*, 1141–1158.

Palmer, C.S., Osellame, L.D., Laine, D., Koutsopoulos, O.S., Frazier, A.E., and Ryan, M.T. (2011). MiD49 and MiD51, new components of the mitochondrial fission machinery. EMBO Rep. *12*, 565–573.

Perkins, G., Renken, C., Martone, M.E., Young, S.J., Ellisman, M., and Frey, T. (1997). Electron tomography of neuronal mitochondria: three-dimensional structure and organization of cristae and membrane contacts. J. Struct. Biol. *119*, 260–272.

Rambold, A.S., Kostelecky, B., Elia, N., and Lippincott-Schwartz, J. (2011). Tubular network formation protects mitochondria from autophagosomal degradation during nutrient starvation. Proc. Natl. Acad. Sci. USA *108*, 10190–10195.

Raucher, D., and Sheetz, M.P. (2000). Cell spreading and lamellipodial extension rate is regulated by membrane tension. J. Cell Biol. *148*, 127–136.

Richardson, W.H. (1972). Bayesian-Based Iterative Method of Image Restoration*. J. Opt. Soc. Am. *62*, 55.

Riggi, M., Bourgoint, C., Macchione, M., Matile, S., Loewith, R., and Roux, A. (2019). TORC2 controls endocytosis through plasma membrane tension. J. Cell Biol. *218*, 2265–2276.

Rooney, J. (2003). Errorbarxy. https://www.mathworks.com/matlabcentral/fileexchange/4065-errorbarxy.

Roux, A., Uyhazi, K., Frost, A., and De Camilli, P. (2006). GTP-dependent twisting of dynamin implicates constriction and tension in membrane fission. Nature *441*, 528–531.

Saitoh, M., Ishikawa, T., Matsushima, S., Naka, M., and Hidaka, H. (1987). Selective inhibition of catalytic activity of smooth muscle myosin light chain kinase. J. Biol. Chem. *262*, 7796–7801.

Schindelin, J., Arganda-Carreras, I., Frise, E., Kaynig, V., Longair, M., Pietzsch, T., Preibisch, S., Rueden, C., Saalfeld, S., Schmid, B., et al. (2012). Fiji: an open-source platform for biological-image analysis. Nat. Methods *9*, 676–682.

Shim, S.H., Xia, C., Zhong, G., Babcock, H.P., Vaughan, J.C., Huang, B., Wang, X., Xu, C., Bi, G.Q., and Zhuang, X. (2012). Super-resolution fluorescence imaging of organelles in live cells with photoswitchable membrane probes. Proc. Natl. Acad. Sci. USA *109*, 13978–13983.

Smirnova, E., Griparic, L., Shurland, D.-L., and van der Bliek, A.M. (2001). Dynamin-related protein Drp1 is required for mitochondrial division in mammalian cells. Mol. Biol. Cell *12*, 2245–2256.

Soleimanpour, S., Colom, A., Derivery, E., Gonzalez-Gaitan, M., Roux, A., Sakai, N., and Matile, S. (2016). Headgroup engineering in mechanosensitive membrane probes. Chem. Commun. (Camb.) *52*, 14450–14453.

Straight, A.F., Cheung, A., Limouze, J., Chen, I., Westwood, N.J., Sellers, J.R., and Mitchison, T.J. (2003). Dissecting temporal and spatial control of cytokinesis with a myosin II inhibitor. Science *299*, 1743–1747.

Tondera, D., Grandemange, S., Jourdain, A., Karbowski, M., Mattenberger, Y., Herzig, S., Da Cruz, S., Clerc, P., Raschke, I., Merkwirth, C., et al. (2009). SLP-2 is required for stress-induced mitochondrial hyperfusion. EMBO J. *28*, 1589–1600.

Trujillo-Ortiz, A. (2015). DagosPtest. https://www.mathworks.com/matlabcentral/fileexchange/3954-dagosptest.

Twig, G., Elorza, A., Molina, A.J.A., Mohamed, H., Wikstrom, J.D., Walzer, G., Stiles, L., Haigh, S.E., Katz, S., Las, G., et al. (2008). Fission and selective fusion govern mitochondrial segregation and elimination by autophagy. EMBO J. *27*, 433–446.

Wang, S., Jiang, C., Zhang, Y., Chen, J., Wang, B., Chen, Q., and Long, M. (2008). Membrane Deformability and Membrane Tension of Single Isolated Mitochondria. Cell. Mol. Bioeng. *1*, 67–74.

Wang, C., Du, W., Su, Q.P., Zhu, M., Feng, P., Li, Y., Zhou, Y., Mi, N., Zhu, Y., Jiang, D., et al. (2015). Dynamic tubulation of mitochondria drives mitochondrial network formation. Cell Res. *25*, 1108–1120.

Wolter, S., Löschberger, A., Holm, T., Aufmkolk, S., Dabauvalle, M.C., van de Linde, S., and Sauer, M. (2012). rapidSTORM: accurate, fast open-source software for localization microscopy. Nat. Methods *9*, 1040–1041.

Yang, C., and Svitkina, T.M. (2019). Ultrastructure and dynamics of the actin-myosin II cytoskeleton during mitochondrial fission. Nat. Cell Biol. *21*, 603–613.

York, A.G., Chandris, P., Nogare, D.D., Head, J., Wawrzusin, P., Fischer, R.S., Chitnis, A., and Shroff, H. (2013). Instant super-resolution imaging in live cells and embryos via analog image processing. Nat. Methods *10*, 1122–1126.

Youle, R.J., and van der Bliek, A.M. (2012). Mitochondrial Fission, Fusion, and Stress. Science *337*, 1062–1065.

STAR★METHODS

KEY RESOURCES TABLE

REAGENT or RESOURCE	SOURCE	IDENTIFIER
Chemicals, peptides, and recombinant proteins		
Blebbistatin	Sigma-Aldrich	B0560
Nocodazole	Sigma-Aldrich	M1404
ML-7 hydrochlorine	Santa Cruz Biotechnology	110448-33-4
Mito-FliptR	Spirochrome	SC023
TMRE	ThermoFisher Scientific	T669
MitoTracker Red CMXRos	ThermoFisher Scientific	M7512
FBS	HyClone	SV30160.03
Opti-MEM	ThermoFisher Scientific	31985062
Lipofectamine 2000	ThermoFisher Scientific	11668030
DMEM	ThermoFisher Scientific	31966021
Leibovitz medium	ThermoFisher Scientific	21083027
PBS	ThermoFisher Scientific	70013016
Glucose oxidase	Sigma-Aldrich	G7141
Catalase	Sigma-Aldrich	C1345
HEPES	ThermoFisher Scientific	15630
Experimental models: Cell lines		
Cos 7 cell line	HPA culture collections	COS7-ECACC-87021302
Recombinant DNA		
Mito-GFP (Cox8 presequence)	Gift from Hari Shroff	N/A
mCherry-Drp1	Friedman et al., 2011	Addgene #49152
MitoBFP	Friedman et al., 2011	Addgene #49151
Dyn2-GFP	Gift from Gia Voeltz	N/A
KDEL-RFP (adapted from KDEL-BFP)	Friedman et al., 2011	Addgene #49150
Software and algorithms		
MATLAB	MathWorks	2016b
Fiji (ImageJ)	(Schindelin et al., 2012), NIH	https://imagej.net/Fiji
Trainable Weka Segmentation	Arganda-Carreras et al., 2017	3.2.33
Structured illumination microscopy simulator	Alharbi, 2013	Alharbi, 2013
MitoWorks	This study	https://github.com/LEB-EPFL/MitoWorks

RESOURCE AVAILABILITY

Lead contact

Further information and requests for resources and reagents should be directed to and will be fulfilled by the Lead Contact, Suliana Manley (suliana.manley@epfl.ch)

Materials availability

This study did not generate new unique reagents.

Data and code availability

Original data used in this study suliana.manley@epfl.ch have been deposited to Zenodo: 10.5281/zenodo.4648097. The custom MATLAB code used to analyze mitochondrial shape, bending energy and tension can be found on the Github repository (https://github.com/LEB-EPFL/MitoWorks).

EXPERIMENTAL MODEL AND SUBJECT DETAILS

African green monkey kidney (Cos-7) cells were grown in Dulbecco's modified Eagle medium (DMEM) supplemented with 10% fetal bovine serum (FBS) at 37°C and 5% CO_2. The Cos-7 cell line was provided by HPA culture collections, which operates with ECACC and uses STR profiling for authentication. Gender of the animal from which Cos-7 cells were derived was not specified upon purchased or independently examined.

METHOD DETAILS

Cell transfections and dye labeling

Cells were plated on 25 mm, #1.5 glass coverslips (Menzel) 16-24 h prior to transfection at a confluency of ~10^5 cells per well. Dual transfections containing mCh-Drp1 (Addgene, plasmid #49152) and Mito-GFP (gift from Hari Shroff, Cox8a presequence) were performed with either Lipofectamine 2000 (Life Technologies) or using electroporation (BioRad Xcell). Lipofectamine transfections were carried out in Opti-MEM using 150 ng of mCh-Drp1, 150 ng of Mito-GFP and 1.5 μL of Lipofectamine 2000 per 100 μL Opti-MEM. Electroporation was performed using salmon sperm as a delivery agent. Briefly, cells were pelleted by centrifugation and resuspended in OPTI-MEM. Plasmids and sheared salmon sperm DNA were added to 200 μL of the cell suspension prior to electroporation using a Bio-Rad Gene Pulser (190 Ω and 950 μFD).

Triple transfections containing mCh-Drp1, Mito-BFP (Addgene, plasmid #49151) and Dyn2-GFP (gift from Gia Voeltz) were performed with Lipofectamine 2000. Such transfections were carried out in using 80 ng of mCh-Drp1, 100 ng of Dyn2-GFP and 80 ng of Mito-BFP and 1.5 μL of Lipofectamine 2000. Dual color imaging of dynamin was performed using double transfections of either 100 ng Dyn2-GFP and 150 ng Mito-Scarlet, or 100 ng Dyn2-mCherry and 150 ng Mito-GFP. Triple transfection containing Mito-BFP, Drp1-GFP and KDEL-RFP were performed with Lipofectamine 2000. Such transfections were performed using 100 ng Mito-BFP, 100 ng Drp1-GFP and 100 ng KDEL-RFP. All quantities listed are per well of cells containing 2 mL of culture medium and carried out with Opti-MEM. The Lipofectamine mixture sat for 20 min before its addition to cells.

All imaging conditions were reproduced multiple times, with at minimum 3 replicates per experimental condition.

Drug treatment

Nocodazole was diluted to a stock solution of 10 mM in DMSO. To depolymerize microtubules, cells were incubated with 10μM Nocodazole (Sigma-Aldrich) for 1h before imaging (1 μL Nocodazole per 1000 μL medium). Control cells were incubated with the equivalent volume of DMSO for 1h before imaging (1 μL DMSO per 1000 μL medium).

Blebbistatin was diluted to a stock solution of 50 mM in DMSO. Cells were incubated with 50μM Blebbistatin (Sigma-Aldrich) for 1h before imaging (5 μL Blebbistatin per 1000 μL medium). Control cells were incubated with the equivalent volume of DMSO for 1h before imaging (5 μL DMSO per 1000 μL medium).

ML-7 was diluted to a stock solution of 50 mM in DMSO. Cells were incubated with 50μM ML-7 (Santa Cruz Biotechnology) for 1h before imaging (5 μL ML-7 per 1000 μL medium). Control cells were incubated with the equivalent volume of DMSO for 1h before imaging (5 μL DMSO per 1000 μL medium).

All drug experiments and controls were reproduced multiple times, with a minimum of three replicates per condition. For each replicate, a minimum of five cells were measured.

FliptR synthesis

The FliptR probe was synthesized following previously reported procedures (Colom et al., 2018). For mitochondrial targeting, compounds 2,3 and 5 were synthesized and purified according to reported procedures (Goujon et al., 2019) (Figure S3B). Figure S3 The probe is also commercially available from Spirochrome.

The probe can report on membrane tension as reported in Colom et al. (2018). Spectroscopic characterizations, mechanosensitive behavior in LUVs and GUVs of various lipid compositions, colocalization studies in mitochondria and response of fluorescence lifetime to osmotic shocks (i.e., membrane tension changes) have been performed (Goujon et al. (2019)).

Microscopy and image reconstruction

SIM imaging and reconstruction

Fast dual-color SIM imaging was performed at Janelia Farm (Fiolka et al., 2012) with an inverted fluorescence microscope (AxioObserver; Zeiss) using an SLM (SXGA-3DM; Fourth Dimension Displays) to create the illumination pattern and liquid crystal cell (SWIFT; Meadowlark) to control the polarization. Fluorescence was collected through a 100X 1.49 NA oil immersion objective and imaged onto a digital CMOS camera (ORCA-Flash4.0 v2 C11440; Hamamatsu). Time-lapse images were acquired every 1 s for 3-5 min, with 50 ms exposure time. Fast dual color imaging of mitochondria and Drp1 was performed at 37°C with 5% CO2, in pre-warmed DMEM medium. Dual-color SIM imaging for Nocodazole and Dyn2 experiments was performed on an inverted fluorescence microscope (Eclipse Ti; Nikon) equipped with an electron charge coupled device camera (iXon3 897; Andor Technologies). Fluorescence was collected with through a 100x 1.49 NA oil immersion objective (CFI Apochromat TIRF 100XC Oil; Nikon). Images

were captured using NIS elements with SIM (Nikon) resulting in temporal resolution of 1 s for single-color and 6-8 s for dual-color imaging, with 50 ms exposure time. Imaging was performed at 37°C in pre-warmed Leibovitz medium.

SIM images were reconstructed using a custom 2D linear SIM reconstruction software obtained at Janelia farm, as previously described (Gustafsson, 2000; Gustafsson et al., 2008). Images were reconstructed using a generalized Weiner filter parameter value of 0.02-0.05 with background levels of ~100.

iSIM imaging and reconstruction

For iSIM experiments (Figure S3A), imaging was performed on a custom-built microscope setup as previously described (Curd et al., 2015; York et al., 2013). The microscope was equipped with a 1.49 NA oil immersion objective (APONXOTIRF; Olympus), with 488 nm and 561 nm excitation lasers and an sCMOS camera (Zyla 4.2; Andor). Images were captured at 0.1-0.3 s temporal resolution for both channels. All imaging was performed at 37°C in pre-warmed Leibovitz medium. Raw iSIM images were deconvolved using the Lucy-Richardson deconvolution algorithm (Lucy, 1974; Richardson, 1972) implemented in MATLAB, run for 40 iterations.

Confocal imaging

Confocal imaging was performed on an inverted microscope (DMI 6000; Leica) equipped with hybrid photon counting detectors (HyD; Leica). Fluorescence was collected through a 63x 1.40 NA oil immersion objective (HC PL APO 63x/1.40 Oil CS2; Leica). Images were captured using the LAS X software (Leica). All imaging was performed at 37°C in pre-warmed Leibovitz medium.

STORM imaging and reconstruction

For STORM imaging (Figure S2A–S2C), prior to staining, cells were washed with PBS (Sigma). Cells were incubated with MitoTracker Red CMXRos (LifeTechnologies) at a concentration of 500 nM for 5 minutes, before washing again with PBS.

For measuring mitochondrial membrane potential, cells were incubated with 100 nM TMRE (Abcam, ab113852) for 10 minutes before time-lapse measurements.

STORM imaging was performed at room temperature in a glucose-oxidase/catalase (Glox) oxygen removal buffer described previously (Shim et al. (2012)). Briefly, a 2% glucose solution is prepared in DMEM (GIBCO). Glucose oxidase (0.5 mg/mL) and catalase (40 μg/mL) were added to the glucose solution and the pH was left to drop for 30-60 min. After this time, the pH was adjusted to 7 yielding a final solution with 6.7% HEPES. Imaging was performed on an inverted microscope (IX71; Olympus) equipped with a 100x NA 1.4 oil immersion objective (UPlanSAPO100X; Olympus) using an electron multiplying CCD camera (iXon+; Andor Technologies), with a pixel size of 100 nm. Laser intensities were between 1-5 $kWcm^{-2}$.

For STORM datasets, single molecules were localized using the RapidSTORM v3.3 software (Wolter et al., 2012). Local signal-to-noise detection with a threshold value of 50 was used. Peaks with a width between 70-300 nm and at least 200 photons were rendered for the final STORM image.

FLIM acquisition and analysis

For FLIM imaging with the mitochondria-targeted FliptR probe, cells were incubated with 500 nM of the probe solution for 15 min, and images without washing. Imaging was performed using a Nikon Eclipse TI A1R microscope equipped with a time-correlated single-photon counting module from PicoQuant. Imaging was performed at 37°C, with 5% CO_e in standard growth medium. A pulsed 485 nm laser (PicoQuant LDH-D-C-485) was used for excitation, operated at 20 MHz. The emission was collected through ha 600/50 nm bandpass filter, on a gated PMA hybrid 40 detector and a PicoHarp 300 board (PicoQuant).

FLIM data was analyzed using the SymPhoTime 64 software (PicoQuant). To determine the fluorescence lifetimes, the fluorescence decay data was fit to a double exponential model after deconvolution for the calculated impulse response function. The values reported in the main text are the average lifetime intensity.

QUANTIFICATION AND STATISTICAL ANALYSIS

Quantifying presence of ER, Dyn2 or Drp1

To assess the presence of different components of the division machinery at mitochondrial constrictions, line profiles were drawn along the length of the mitochondrion by hand with a 5 pixel thickness using Fiji (Schindelin et al., 2012). The presence of one of these components was marked by a signal > 3 times above background levels within 1 μm of the construction site (marked by a dip in the mitochondrial marker).

Quantification of rounds of Drp1 constriction

To count the number of rounds of constriction by Drp1, we superimposed the normalized Drp1 intensity with the constriction diameter. Local maxima in the normalized Drp1 signal that overlapped with a constriction diameter < 200 nm marked a round of constriction, which ended either in a decrease of Drp1 accompanied by a diameter > 200 nm, or by fission.

Mitochondrial shape and motion analysis

Images were first segmented using the open-source software ImageJ/Fiji (https://fiji.sc) and the Weka Segmentation V3.2.17 plugin (Arganda-Carreras et al., 2017) with the resulting probability map used as the segmented image. Subsequent analysis was performed using a custom MATLAB functions which contoured the mitochondria and created a backbone with a mesh. This allowed us to measure the diameter and curvature along the constricted mitochondrion, and hence estimate the local bending energy. Tracking the

position of the constriction site allowed us to measure the local Drp1 intensity. Tracking the leading edge of divided daughter mitochondria was used to estimate the membrane tension prior to fission.

The custom MATLAB package can be found on the Github repository (https://github.com/LEB-EPFL/MitoWorks) and allowed us to perform the summarized steps (Figure S6):

1. mitoTrack: Identify mitochondria in the segmented image and find nearest neighbor mitochondria in the subsequent frame. Mitochondrial tracks are made up of nearest neighbor mitochondrial centers of mass (using the knnsearch function built into MATLAB) in consecutive frames. The tracked mitochondrion of interest is then cropped from both segmented and original time-lapse images for different channels
2. genContour: Create contour of the mitochondrion of interest using a built-in MATLAB function based on Chan-Vase active contouring of the segmented (Chan and Vese, 2001). A small Gaussian filter is applied prior to contouring. The generated contour is then smoothed over a length scale of ~170 nm, which was found to be optimal for eliminating noise without sacrificing envelope curvature sensitivity. Contour smoothing was performed using a third-party function based on least-squares smoothing for MATLAB (Jim, 2015).
3. mitoMesh: Create a backbone, or centerline, of the mitochondrion of interest. The backbone is smoothed over a lengthscale of ~150 nm. Use generated backbone to divide mitochondrion into smaller segments, with the boundaries represented by a mesh, defined by lines drawn perpendicular to the backbone with subpixel spacing.
4. genCurv: measure the curvature along the contour of the mitochondrion using a third party 'LineCurvature2D' function for MATLAB (Kroon, 2011).
5. minDiameterSearch: Use the diameters measured along the mesh to track the position of the constriction site, and measure its diameter.
6. measureBE: Use mesh to measure dimensions of individual segments. For each segment, use the measured diameters and envelope curvatures to estimate the bending energy and bending energy density of that segment. Find the length scale that maximizes the local bending energy density.
7. genFWHM: Generate FWHM based contour by fitting profiles plotted along the mesh with a Gaussian function. Connect the measured widths at along the mitochondrion and smooth at a length scale of ~170 nm to generate the FWHM contour. Repeat minDiameterSearch and measureBE for FWHM contour.
8. measureDrp1: Measure the local Drp1 integrated intensity within a chosen radius around the constriction site. Radii used for all datasets: ~500 nm. Subtract background and bleach correct using a custom-written linear bleach correction function.
9. mitoPull: Repeat genContour and mitoMesh for daughter mitochondria after fission. Track the leading-edge retracting from the constriction site, corrected for the motion of the whole mitochondrion, to estimate membrane tension, using a viscoelastic model (Lafaurie-Janvore et al., 2013). For membrane tensions estimated from recoil motion, the retraction was fit to an exponential decay function (y = a*exp(bx)), and extrapolated to zero.

To compare the snake and FWHM contours we simulated SIM images using a third-party SIM image generator (Alharbi, 2013). Different shapes representing mitochondrial constriction sites at an SNR < 2, the typical value at mitochondrial constriction sites, were simulated and used to generate snake and FWHM contours. We observed that although the measured minimum diameters were comparable between the two contours, the snake contour was better at detecting high envelope curvatures (Figure S6). Hence the analysis was performed on the snake contour.

To quantify morphological features of mitochondria and after nocodazole treatment, SIM time-lapse images before and after nocodazole treatment were analyzed as follows: Mitochondrial membrane potential was analyzed by measuring mean fluorescence intensity of single mitochondria (ROI defined by using Otsu thresholding and Analyze Particles Plugin) on SIM images and subtracting the cytosolic background. The diameter of mitochondria was determined by FWHM measurement profile across individual mitochondria on time-lapse SIM recordings.

Estimating membrane tension using tubules

To estimate mitochondrial membrane tension, we used mitochondrial tubules – short-lived structures pulled out of mitochondria by motor proteins (Huang et al., 2013; Wang et al., 2015). By drawing analogy to membrane pulling experiments (Derényi et al., 2002; Evans and Yeung, 1994), the diameter of the tubule d is a readout for membrane tension τ:

$$d = \sqrt{\frac{2\kappa_B}{\tau}} \Rightarrow \tau = \frac{2\kappa_B}{d^2}$$

Where κ_B is the bending rigidity, taken as 20 kT for a single membrane (Niggemann et al., 1995). The radius of the tube was measured only when the motion of the tube stabilized, and before retraction. Mitochondrial tubules that did not retract and formed a branch on the mitochondrion were not considered.

Estimating membrane tension using retraction speed

We used a visco-elastic model of the retraction of the mitochondrial membrane after fission to estimate the local membrane tension. The same model was used previously to estimate the membrane tension in the intercellular bridge during cytokinesis (Lafaurie-Janvore et al., 2013).

$$\sigma(t) = \int_{-\infty}^{t} \frac{du}{dt}(t = t^*) \times E(t - t^*)dt^* \approx \int_{0}^{t_0} \frac{du}{dt}(t = t_0) \times E(0)dt \approx \frac{v(t_0)}{l_0} \times \eta$$

where σ is the stress, u the strain, E the relaxation modulus. $E(0)$ is approximated as the effective viscosity η at the moment of fission. $v(t_0)$ is the retraction speed at the moment of fission and l_0 the deformation length. l_0 was taken as 250 ± 15 nm (mean ± SEM, n = 78 recoiling mitochondria from 39 fission events), averaged over all observed fissions. The deformation length was measured by comparing the shape of mitochondria before and after fission. The viscosity was taken as 120 cP (Liu et al., 2014).

From there, we find the force F by multiplying the stress by the cross-sectional area A:

$$F = \sigma A \cong \sigma \pi r^2$$

Where r is the constriction radius. The membrane tension τ is then estimated by dividing the pulling force by the circumference at the constriction site:

$$\tau = \frac{F}{2\pi r}$$

This retraction-based tension estimate, determined from recoil velocities reported in the manuscript (Figure 3G), is lower due to low temporal resolution, confirmed by comparing values from faster iSIM imaging (Figure S4J). Regardless, this method reports a real relative difference in membrane tensions of fission events between control and nocodazole treated cells.

Estimating bending energy

To determine the area over which to measure the bending energy, we determined for the length scale that maximized the local bending energy density. This was done by considering areas composed of increased numbers of segments around the constriction site (Figure S4D). The appropriate length scale was then selected by finding the area at which the bending energy density (ratio of bending energy and area) was maximal (Figures S4F and S4J). The bending energy was then considered at this length scale. The length scales did not differ significantly between fissions and reversals (Figure S4H).

The following equation was then integrated over the area corresponding to the appropriate length scale, to find the bending energy (Helfrich, 1973) E_B:

$$E_B = \frac{\kappa_B}{2} \int J^2 dA$$

Where κ_B is the bending rigidity, J the sum of local principal curvatures along the constriction site and A the surface area of the constriction site. The bending rigidity taken to be ~20 kT, as previously reported for lipid bilayers (Niggemann et al., 1995). Since we consider a double-membrane system, we take the value of κ_B = 40 kT.

The above equation was applied to a discretized contour of mitochondria. The contour was subdivided into small segments sampled every ~15 nm. The tube curvature was determined by calculating the average radius of the segment. The envelope curvature was taken as the weighted average of the two envelope curvatures, located at each side of the segment. The envelope curvatures were weighted by the length of each side of the segment, and assumed to vary linearly across the two sides of the segment. Finally, to calculate the surface area of the segment, we approximated the shape of the segment as a truncated cone. Therefore, for a single segment, the bending energy was given by:

$$E_B = \frac{\kappa_B}{2} \cdot \left[\frac{1}{\langle R_t \rangle_{seg}} + \frac{1}{l_1 + l_2} \left(\frac{l_1}{\langle R_{e,1} \rangle_{seg}} + \frac{l_2}{\langle R_{e,2} \rangle_{seg}} \right) \right]^2 \cdot \left[\pi (R_{t,1} + R_{t,2}) \sqrt{(R_{t,1} - R_{t,2})^2 + h^2} \right]$$

Where $\langle R_t \rangle_{seg}$ is the average tube radius across the segment, l_1 and l_2 the side lengths of the two sides of the constriction site, $\langle R_{e,1} \rangle_{seg}$ and $\langle R_{e,2} \rangle_{seg}$ the average envelope curvatures of the two sides of the constriction site, $R_{t,1}$ and $R_{t,2}$ the edge tube radii of the segment and h the average length through the center of the segment (Figure S4).

Estimating energy barrier to fission and fluctuation energy

Stochastic model for fission

Given a membrane bending energy E∈ [0,E_f], thermal fluctuations allow membranes to stochastically overcome the residual energy barrier ΔE to fission, with probability p(E) for energy barrier (Morlot et al., 2012),

$$p(E) = exp\left(-\frac{\Delta E}{\lambda}\right) = exp\left(\frac{E - E_f}{\lambda}\right)$$

Where in the case of thermal fluctuations, $\lambda = k_B T$. Fitting the measured experimental probability of fission (Figure 4A) to the equation above, allowed us to estimate the fluctuation energy $\lambda \sim 90\ k_B T$ and the energy barrier to fission $E_f \sim 250\text{-}300\ k_B T$ .Fitting the equation above to control and nocodazole-treated cells indeed shows that while the barrier to fission remains mostly unchanged, the size of the energy fluctuations was decreased 6-fold in the nocodazole-treated condition (Figure 4B).

Estimating fluctuation transduction between inner and outer mitochondrial membranes

From our model, the fission probability is set by two factors: the distance from the energy barrier set by the bending energy and the size of the available fluctuations arising from membrane tension. Each factor was considered separately.

By assuming a constant distance d between the two mitochondrial membranes (d ≈ 22 nm; Perkins et al., 1997), we can relate the local principal curvatures of the outer mitochondrial membrane to the inner as follows (i denotes the inner mitochondrial membrane and o the outer mitochondrial membrane) (Figure S5A):

$$R_{e,i} = R_{e,t} + d$$

$$R_{t,i} = R_{t,o} - d$$

Where R_e and R_t are the envelope and tube radii of curvature respectively. This is supported by the observation from electron microscopy that cristae are excluded from constriction site (Hu, 2014). From this we can compute a readout for the bending energy density at a single point along the membrane (neglecting the bending rigidity κ) (Figure S5B):

$$\varepsilon_b = \left(\frac{1}{R_e} + \frac{1}{R_t}\right)^2$$

The inner mitochondrial membrane will intrinsically have a higher bending energy and will therefore be closer to the energy barrier to fission (smaller residual energy ΔE). By comparing the bending energies of the two membranes, we can see that on average the inner membrane will have almost a two-fold higher bending energy (Figure S5C).

Any membrane tension-inducing force arising from the surroundings acting on the mitochondria is exerted through the outer mitochondrial membrane. We expect that coupling, which could arise from proteins spanning the two membranes such as Tim23 (Donzeau et al., 2000), transduces a part of the force from the outer to the inner membrane.

The probability of fission P is related to the residual energy (distance to the energy barrier) ΔE, and the inverse of the fission time t_f by:

$$P \propto \frac{1}{t_f} \propto \exp\left(-\frac{\Delta E}{\lambda}\right)$$

Where λ reflects the magnitude of the fluctuations. We introduce a coupling variable ω∈ [0,1] such that $\lambda_i = \omega\lambda_o$ where λ_i reflects the fluctuations transduced to the inner membrane from the outer membrane (λ_o). In this case, we can express the probabilities as

$$P_o \propto \frac{1}{t_{f,o}} \propto \exp\left(-\frac{\Delta E}{\lambda_o}\right)$$

$$P_i \propto \frac{1}{t_{f,i}} \propto \exp\left(-\frac{\Delta E}{\lambda_i}\right) = \exp\left(-\frac{\Delta E}{\omega\lambda_o}\right)$$

We can then express P_i as a function of P_o and ω, where the constant of proportionality is 1:

$$P_i = P_o^{1/\omega}$$

In this case, (ω = 1), the inner mitochondrial membrane will always be less likely to undergo fission than the outer (Figure S5D). The inner mitochondrial membrane would therefore need to achieve higher energies to overcome the energy barrier, given the lower scale of available fluctuation energies.

We can compute again the probability of fission for the two mitochondrial membranes:

$$P_o \propto \frac{1}{t_{f,o}} \propto \exp\left(-\frac{\Delta E}{\lambda_o}\right)$$

$$P_i \propto \frac{1}{t_{f,i}} \propto \exp\left(-\frac{\Delta E}{\lambda_i}\right) = \exp\left(-\frac{\Delta E}{\omega\mu\lambda_o}\right)$$

Where μ represents the ratio of residual energies. This implies that the inner mitochondrial membrane can still have a higher probability of fission, even if the coupling to the outer membrane is not perfect (Figures S5E and S5F) and therefore will be more likely to undergo fission (Figures S5E and S5F). For factors of $\mu > 1$, there will exist cases of imperfect coupling ($\omega < 1$), which will still give the inner and outer membranes equal fission probabilities (Figures S5G–S5I). Furthermore, for a fixed ratio of bending energies μ we can identify 3 regimes: (I) $P_i < P_o$ below a critical coupling ($\omega < \omega_c$), (II) $P_i > P_o$ for ($\omega > \omega_c$), and (III) $P_i = P_o$ at critical coupling ($\omega = \omega_c$).

The necessary coupling for a combination of P_i, P_o, μ can be found as:

$$\omega = \frac{\log P_o}{\mu \log P_i}$$

Therefore, as the inner membrane gets relatively closer to the energy barrier (increasing μ), the required coupling will decrease (Figures S5J–S5L). Critical coupling, ω_c, corresponding to $P_i = P_o$ is given by:

$$\omega_c = \frac{1}{\mu}$$

Therefore, even in cases where the coupling is not perfect ($\omega < 1$), our model predicts that the inner membrane can still undergo fission first. Furthermore, in reality the ratio of bending energies μ is expected to be even higher than 2, suggesting that the regime where the inner membrane undergoes fission first can exist at even much lower degrees of coupling.

Estimating the energetic contribution of membrane tension

The contribution of stretching energy was found from two independent estimates below:

Method 1: Estimating stretching energy associated with measured membrane tensions

Based on mitochondrial geometry and measured membrane tension values, we calculate the stretching energy. We perform a calculation of the stretching energy based on the measured membrane tension values from iSIM data and mitochondrial tubules ($\sim 4.10^{-6}$N/m). Stretching energy E_τ due to membrane tension τ and change in surface area ΔA, can be estimated as:

$$E_\tau = \tau \Delta A$$

By modeling a mitochondrion as a cylinder with diameter 1 μm and length 5 μm, and assuming a 0.3% stretch factor (Helfrich, 1973; Wang et al., 2008), we estimated $\Delta A \approx 0.05\ \mu m^2$. Combining this estimate with the membrane tension estimate ($\sim 4.10^{-6}$ N/m), we obtain that the average energy contribution is $\sim$50 kT.

Method 2: Experimental estimation of stretching energy

When tension is applied to a membrane, it causes a change in area resulting in a stretching energy E_τ. Since stretching energy E_τ scales linearly with membrane tension τ, we have:

$$E_\tau \propto \tau \Rightarrow E_\tau = \alpha\tau \Rightarrow \alpha = \frac{dE_\tau}{d\tau} \cong \frac{\Delta E_\tau}{\Delta\tau}$$

We can therefore approximate the constant of proportionality α by looking at the change in stretching energy produced by a change in membrane tension. Specifically, we compared the difference in mean bending energies and mean membrane tensions between control and nocodazole treated cells (Figures 4B and 4C). We estimated the energy due to membrane tension E_τ as:

$$E_\tau = \left|\frac{\Delta E}{\Delta\tau}\right| \tau_{ctrl} = \left|\frac{E_{noco} - E_{ctrl}}{\tau_{noco} - \tau_{ctrl}}\right| \tau_{ctrl}$$

Where E_{noco}, E_{ctrl} are bending energies for nocodazole-treated and control cells respectively, τ_{noco}, τ_{ctrl} the membrane tensions for nocodazole-treated and control cells respectively. This gives a value of E_τ of 40 kT, consistent with estimate 1 above.

Estimating fission time

To estimate the time of fission (Figure 4D), we examined the evolution of the constriction site diameter and local Drp1 intensity. The fission time was then taken as the offset of the final increase of Drp1 and decrease in constriction diameter, which should correspond to the constriction time before fission (Figure S1).

Statistics

Statistics were performed using MATLAB and OriginPro software. All datasets were tested for normal distribution using the D'Agostino-Pearson normality test (significance value of 0.05) (Trujillo-Ortiz, 2015). If the datasets passed the test, then statistical significance was determined using a two-tailed t tests. If datasets failed the normality test, a nonparametric test was chosen to compare the significance of means between groups Mann-Whitney test for two samples (with one or two tailed distributions where appropriate) and Kruskal-Wallis ANOVA for multiple samples (Cardillo, 2015). $p < 0.05$ were considered as significant and were marked by '*'; $p < 0.01$ with '**', $p < 0.001$ by '***' and $p < 0.0001$ by '****' and can be found in the figure legends.

Sample sizes are reported as n within the manuscript or figure legends. Unless otherwise noted, graphs show mean values and error bars represent the standard deviation. All plots in this work were generated using a third-party function for MATLAB to generate shaded areas representing standard error (Rooney, 2003).